PERGAMON

International Journal of Heat and Mass Transfer 44 (2001) 1285–1297

International Journal of
HEAT and MASS
TRANSFER

www.elsevier.com/locate/ijhmt

Modeling Soret coefficient measurement experiments in porous media considering thermal and solutal convection

L.B. Benano-Melly [a], J.-P. Caltagirone [a,*], B. Faissat [b], F. Montel [b], P. Costeseque [c]

[a] *MASTER-ENSCPB, University Bordeaux I, Av. Pey-Berland, B.P. 108, 33402 Talence, France*
[b] *Elf Aquitaine (Production), CSTJF, Av. Larribau, 64000 Pau, France*
[c] *LMTG, UMR 5563, University Paul Sabatier, 39 Allées Jules Guesde, 31000 Toulouse, France*

Received 7 November 1995; received in revised form 25 May 2000

Abstract

We address the problem of thermal diffusion in binary fluid mixtures, lying within a porous medium and subjected to a horizontal thermal gradient. Preliminary numerical results indicate that multiple convection-roll flow patterns can develop depending on the Soret number value, for counteracting thermal and solutal buoyancy forces. Investigating solute behaviour, the influence of these forces on solute transport is described in detail. Furthermore, it is shown that the theory represents well the solute behaviour when solutal buoyancy force is negligible. Finally, reproducing thermo-gravitational experiments by numerical means, dispersion is exhibited as a possible cause of the observed discrepancy between numerical and experimental results. The influence of dispersion on diffusive and thermal diffusive solute transports can be strong. © 2001 Elsevier Science Ltd. All rights reserved.

1. Introduction

Thermal diffusion, also called solutal thermodiffusion or the Soret effect [1], corresponds to species differentiation, developing in an initially homogeneous mixture submitted to a thermal gradient. Although usually considered as a second-order phenomenon, the importance of thermal diffusion is becoming more widely accepted; examples are in geosciences when considering magma differentiation [2–4], in hydrology when studying mineral enrichment of geothermal sources [5,6] or, although some disagree [9], in petrology when investigating hydrocarbon segregation [7,8].

Theoretical developments regarding solutal thermodiffusion have been achieved by Furry et al. [10] for binary mixtures, and more generally by De Groot [11] and De Groot and Mazur [12] by means of irreversible process thermodynamics. They exhibit the driving force for the phenomenon, ∇T, and the governing coefficient, called thermal diffusion coefficient, D^t. Compositional gradients and species behaviour not only depend on the existing temperature gradient, but also on D^t value (D^t being specific to each mixture component).

Most studies carried out on this topic deal with binary mixtures. Soret number, $S^t = D^t/D$ allowing the comparison of fickian to thermal diffusion, is then often used and measured instead of D^t. Usually, the mixture heaviest component migrates to the cold side, and if the mixture components are of the same mass, the larger molecules migrate to the cold side [13]. The Soret number is then positive. However, in some cases, the component migrating towards the cold side is the lighter one and the Soret number is negative.

Among the studies carried out to understand how the Soret effect acts on heat transfer and mass transport in binary mixtures, several configurations have been considered.

Many deal with mixtures in a strictly fluid cell (no porous medium inside the cell) submitted to a vertical thermal gradient with the cell bottom being the cell hot side [14–17]. By means of stability analysis, the action of thermal diffusion on bifurcations in Bénard convection problems is determined. Hence, it has been shown

---

[*] Corresponding author.

PII: S0017-9310(00)00183-6

Nomenclature

a	reference thermal diffusivity
$\mathscr{A}$	transport parameter
$\mathscr{B}$	transport parameter
c	concentration
$\mathscr{C}$	transport parameter
C_{p}	heat capacity
D	diffusion coefficient
D_{d}	diffusion–dispersion coefficient
D^{t}	thermal diffusion coefficient
$D^{\mathrm{t}}_{\mathrm{d}}$	thermal diffusion–dispersion coefficient
F_{s}	solutal buoyancy force
F_{t}	thermal buoyancy force
H	cell height
$\mathscr{H}$	transport parameter
$HA = L/H$	cell aspect ratio
J_i	mass flux of species i
J_i^{c}	convective flux of species i
J_i^{f}	diffusive flux of species i
J_i^{s}	thermal diffusive flux of species i
k	permeability
$\mathscr{K}$	transport parameter
L	cell length
Le	Lewis number
m_x	solute mass transport along axis x
$\mathbf{n}$	cell-wall normal unit vector
$\mathbf{n}_{\mathrm{g}}$	unit vector along gravity direction
p	pressure
q	separation ratio
Ra^{s}	solutal Rayleigh number
Ra^{t}	thermal Rayleigh number
Sc	Schmidt number
S^*	critical Soret number
S	dimensionless Soret number
S^{t}	dimensioned Soret number
t	time
T	temperature
V	velocity

Greek symbols

α	solutal expansion coefficient
β	thermal expansion coefficient
λ	heat conductivity
ϕ	porosity
ρ	density
μ	dynamic viscosity
ν	cinematic viscosity

Subscripts

0	reference quantities
c	cold
eq	equivalent quantities
f	fluid
h	hot
i	species ($i = 1, 2$)
m	optimum
s	solute

Superscripts

eq	equivalent quantities
num	numerical
$*$	dimensioned quantities

[18,19] that a threshold value, $S^* < 0$, exists for the Soret number, S^{t}, such that: for $S^{\mathrm{t}} < S^*$ oscillatory convection develops, for $S^{\mathrm{t}} > S^*$ steady convection occurs and $S^{\mathrm{t}} = S^*$ corresponds to a codimension two-point (Hopf bifurcation). Zimmermann and Müller [14] experimentally visualise these flow patterns and describe lean component transport along streamlines within a moving convection roll.

Other works consider thermal diffusion induced by a horizontal thermal gradient (also in a strictly fluid cell) [13,20,21]. Bergman and Srinivasan [20] numerically describe the flow patterns developing within a square-shaped cell, and show that counteracting solutal and thermal buoyancy forces ($S^{\mathrm{t}} < 0$) often lead to heat transfer dominated by conduction. Furthermore, they show the importance of the Soret effect at low thermal Rayleigh number, while Weaver and Viskanta [13] show the importance of thermal diffusion on mass transfer in general (10–15% of the total mass flux).

Parallel to these, other studies are devoted to Soret number calculation, either by means of molecular dynamics [22] or using experimental devices. In the latter, Soret number can be evaluated either using optical apparatus [23,24] or measuring species differentiation within a thermal diffusion cell [25,26]. Originally used by Clusius and Dickel [27,28], the thermogravitational diffusion effect has been used in thermal diffusion cells containing a porous medium to control convection. In these devices the mixture is submitted to a horizontal thermal gradient and results have been obtained for Soret number of different species in binary mixtures [6,29].

Hitherto, to the authors knowledge, thermogravitation in binary mixtures has not been intensively investigated by numerical means, although the importance of the Soret effect has been shown, as we have seen, in many situations, and can be assumed in many others (for example hydrocarbon segregation in oil or gas fields). Jamet et al. [30] attempted to numerically handle this problem. However, plotting cell-bottom to cell-top solute-concentration ratio versus the log of permeability, they noted a discrepancy between numerical and experimental results. Their study shows that a permeability anisotropy could not be responsible for this discrepancy.

We are therefore numerically addressing the problem of thermogravitation in binary fluid mixtures. Our goal is to reproduce Soret number measurement experiments and explain the discrepancy already observed between numerical and experimental results [30]. First, a mathematical description of the problem is given. Then, we propose a flow description, and a short heat transfer and mass transport analysis, which will help in extracting the parameters relevant to the maximum separation obtained in thermogravitational cells. Finally, we aim to reproduce some of the Soret number measurement experiments done using thermogravitational cells [6] and discuss the results obtained.

2. Problem formulation

Fig. 1 shows, schematically, the thermogravitational cell under study. The walls are impermeable to matter. The vertical walls are set to constant yet different temperatures, T_h and T_c, while the top and bottom are adiabatic walls. The binary mixture filling the cell porous medium (permeability k, porosity ϕ) is initially homogeneous. Hence, due to the thermal gradient, fluid undergoes convection and mixture species are submitted to the Soret effect.

The governing equations for the problem follow. No chemical reaction occurs between the species and no interactive superficial force acts between the porous medium particles and the liquid mixture (capillary or Marangoni forces are neglected). There must be conservation of the total mass (Eq. (1), assuming incompressible flow) and of each species i (Eq. (2)). Darcy's law is valid for the fluid (Eq. (3)) and energy conservation is represented by Eq. (4). Furthermore, we consider the following state law for the fluid: fluid density, ρ_f^*, is a linear function of temperature, T^*, and solute concentration, c_s^* (Eq. (5))

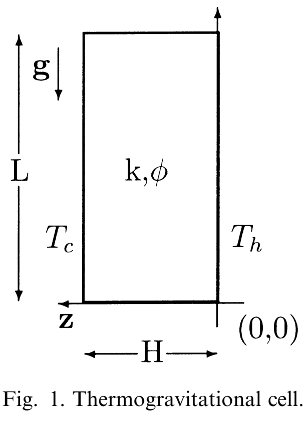

Fig. 1. Thermogravitational cell.

$$\nabla \cdot V_f^* = 0, \tag{1}$$

$$\phi \frac{\partial \rho_i^*}{\partial t^*} + \nabla \cdot (\rho_i^* V_i^*) = 0, \tag{2}$$

$$V_f^* = -\frac{k}{\mu}(\nabla p^* - \rho_f^* g), \tag{3}$$

$$(\rho C_p)_{eq}^* \frac{\partial T^*}{\partial t^*} + (\rho C_p)_f V_f^* \nabla T^* = \nabla \cdot (\lambda_{eq}^* \nabla T^*), \tag{4}$$

$$\rho_f^* = \rho_{f_0}(1 - \beta(T^* - T_0) + \alpha(c_s^* - c_{s_0})). \tag{5}$$

Subscript 0 denotes reference quantities evaluated at mean temperature $T_0 = 0.5(T_h + T_c)$, subscript eq denotes equivalent quantities for the set solid–matrix/mixture, and subscript f denotes quantities relative to the mixture. α and β are the fluid phase solutal and thermal expansion coefficients, respectively.

Eq. (2) can be modified to express conservation of each species in terms of its concentration, $c_i^* = \rho_i^*/\rho_f^*$, noting that total flux of species i ($J_i = \rho_i^* V_i^*$) is due to a convective flux of i ($J_i^c = \rho_f^* c_i^* V_f^*$), a Fickian diffusive flux of i ($J_i^f = \rho_f^* D_i^* \nabla c_i^*$) and a thermal diffusive flux of i ($J_i^s = \rho_f^* D_i^{t^*} c_i^* \nabla T^*$).

Hence, writing solute conservation within the cell leads to Eq. (6), which is used instead of Eq. (2) (second mixture-component concentration is equal to $1 - c_s^*$). Note that solute Soret number, S^t, appears in this equation

$$\phi \frac{\partial c_s^*}{\partial t^*} + \nabla \cdot (c_s^* V_f^*) = \nabla \cdot (D_s^* \nabla c_s^*) + \nabla \cdot (S^t D_s^* c_s^* \nabla T^*). \tag{6}$$

Boundary conditions are no flow and no mass flux through the cell walls, constant temperature, T_c and T_h, on each of the vertical walls, and no heat flux through the horizontal walls.

Normalised equations are used (Eqs. (7)–(10), the equation of state for the fluid being introduced in Darcy's law)

$$\nabla \cdot V_f = 0, \tag{7}$$

$$\phi \frac{\partial c_s}{\partial t} + \nabla \cdot (c_s V_f) = \frac{1}{Le} \nabla \cdot (D_s \nabla c_s) + \frac{1}{Le} \nabla \cdot (S D_s c_s \nabla T), \tag{8}$$

$$V_f = -\nabla p + Ra^t T \mathbf{n}_g - Ra^s (c_s - 1) \mathbf{n}_g, \tag{9}$$

$$\xi \frac{\partial T}{\partial t} + V_f \nabla T = \nabla \cdot (\lambda_{eq} \nabla T), \tag{10}$$

where $\mathbf{n}_g$ is the unit vector along axis x (see Fig. 1), and $\xi = (\rho C_p)_{eq}/(\rho C_p)_f$. The unknowns are the following dimensionless variables:

$$T = \frac{T^* - T_0}{T_h - T_c}, \quad c_s = c_s^*/c_{s_0}, \quad \rho = \rho^*/\rho_0, \\ V = \frac{H}{a}V^*, \quad t = \frac{a}{H^2}t^*, \quad p = \frac{\rho_0 a^2}{H^2}p^*, \tag{11}$$

where superscript $*$ denotes the dimensioned quantities appearing in Eqs. (1)–(5) and $a = \lambda_0^{eq}/(\rho_0 C_p)_f$ is a reference thermal diffusivity. Distances are normalised using H as the reference length, and other physical parameters are normalised using their value at temperature T_0. The dimensionless parameters appearing in Eqs. (7)–(10) follow:

Thermal Rayleigh number:

$$Ra^t = \frac{\rho_0 g \beta \Delta T k H}{\mu a},$$

Solutal Rayleigh number:

$$Ra^s = \frac{\rho_0 g \alpha c_0 k H}{\mu D_{s_0}},$$

Lewis number:

$$Le = \frac{a}{D_{s_0}},$$

Normalised Soret number:

$$S = S^t \Delta T,$$

where $\Delta T = T_h - T_c$ and D_{s_0} is the solute diffusion coefficient at temperature T_0. The corresponding normalised boundary conditions are:

$$\begin{cases} V_f \cdot \mathbf{n} = 0 \quad \text{and} \quad \dfrac{\partial c_s}{\partial \mathbf{n}} + Sc_s\dfrac{\partial T}{\partial \mathbf{n}} = 0 \text{ through each wall}, \\ T(z=1) = T_c \quad \text{and} \quad T(z=0) = T_h, \\ \dfrac{\partial T}{\partial \mathbf{n}} = 0 \quad \text{at } x = 0 \text{ and } x = L/H, \end{cases}$$

where $\mathbf{n}$ is the considered wall normal unit-vector.

3. Numerical method

The time discretisation scheme is semi-implicit: buoyancy terms in Eq. (7) are explicitly treated. An augmented Lagrangian method [31], based on the Uzawa algorithm [32], is then used to solve the fluid flow Eqs. (7) and (9). The aim of this procedure is to find a pressure field responsible for a velocity field that verifies the incompressibility constraint: $\nabla \cdot V_f = 0$. The calculation will proceed in the following way:

Knowing pressure and velocity fields at a given timestep (say n) L iterations:

1. Calculate $V_f^{(n+(l/L))}$ using:

$$V_f^{(n+(l/L))} + r\nabla\left(\nabla \cdot V_f^{(n+(l/L))}\right) = -\nabla p^{(n+(l-1)/L)} + \mathbf{F}. \tag{12}$$

2. Calculate $p^{(n+(l/L))}$ using:

$$p^{(n+(l/L))} = p^{(n+(l-1)/L)} - \xi\nabla \cdot V_f^{(n+(l/L))}. \tag{13}$$

3. If $\nabla \cdot V_f^{(n+(l/L))} > \varepsilon$ go back to 1

Convergence is reached when $\nabla \cdot V_f^{(n+(l/L))} \leqslant \varepsilon$ (say for $l = L$, ε being small).

The parameters r and ξ are chosen appropriately to accelerate convergence: because we are operating with normalised quantities, these parameters take values close to 1. In Eq. (12), $\mathbf{F}$ stands for the buoyancy forces at timestep (n). Once the fluid velocity is known at timestep ($n + 1$), Eqs. (8) and (10) allow the computation of the solute concentration and of the temperature at the same timestep.

This method has two main advantages. First, it permits the iterative solution of the velocity–pressure coupling, which prevents us from having a large and ill-conditioned matrix to solve. Second, there is no need for a boundary condition on pressure. This procedure is quite efficient and has been successfully used by one of the authors to solve fluid flow in many different problems [33–35]. A more detailed description of the augmented Lagrangian method can be found there.

Spatial discretisation of these equations, based on a central difference scheme, is performed on MAC grids: temperature, pressure and concentration are evaluated on main-grid nodes, while velocity components are calculated on staggered grids. It is achieved using finite volumes in accordance with the method described by Patankar [36] for fluid flow. The linear systems obtained for velocity, temperature and concentration are solved using a conjugated gradient method, BiCGStab [37].

4. Results and discussion

4.1. Flow pattern and heat transfer

4.1.1. Flow analysis

We aim at modelling experiments achieved with specific thermogravitational cells [6]. Their aspect ratio is $HA = L/H = 100$. Due to the thermal gradient direction, the mixture undergoes convection. The window in Fig. 2 shows the velocity profiles across the cavity at half the cell height, for different thermal and solutal Rayleigh numbers, when only one convection roll is observed. The positive half of these profiles is shown on a log scale in the same diagram (the value is close to zero at the mid-cell). Convection velocity is higher on the cell vertical

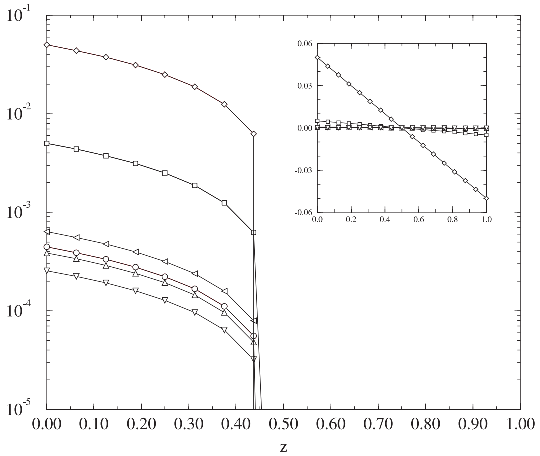

Fig. 2. Convection velocity profiles (window shows profiles on a cartesian scale): ○ $(0, 10^{-3}, 1.2\times10^{-3})$, □ $(0, 10^{-2}, 1.2\times10^{-3})$, ◇ $(0, 10^{-1}, 1.2\times10^{-3})$, △ $(10^{-1}, 10^{-3}, -1.2\times10^{-3})$, ◁ $(10^{-0.5}, 10^{-3}, 1.2\times10^{-3})$, ▽ $(10^{-0.5}, 10^{-3}, -1.2\times10^{-3})$, where $(*, *, *)$ are values for (Ra^s, Ra^t, S).

sides due to the boundary slip condition. This figure shows that the solutal buoyancy force has negligible or no effect on convection for solutal Rayleigh numbers lower than 10^{-1}. This is due to the low value of the term $c_s - 1$ in Eq. (9): $c_s - 1 \leqslant 10^{-2}$ for the thermal Rayleigh numbers considered.

Combined solutal and thermal buoyancy forces. When Ra^s is high enough, for positive Soret numbers, the thermal and the solutal buoyancy forces combine their actions to enhance convection: the higher the Rayleigh numbers, the higher the convection velocity as shown in Fig. 2 (a short explanation on Soret number influence on solutal buoyancy force is given in Section 4.2.1).

Counteracting solutal and thermal buoyancy forces. For negative Soret numbers, the solutal buoyancy force opposes to flow and convection velocity is reduced. In some cases, Ra^s can be so high that solutal buoyancy force is dominant. Convection flow can then change direction or multiple-roll configurations can appear. Fig. 3 shows Ra^s values for which transition occurs, depending on Ra^t.

These results qualitatively agree with the Chock and Li [18] and Zimmerman [19] linear stability analysis, although a direct comparison is impossible because we consider a fluid in porous medium. For a positive Soret number (e.g. greater than its critical value) steady convection occurs (region (I) in Fig. 3), whereas for a negative Soret number stable multiple convection rolls can develop (region (III) in Fig. 3). In addition to this, the numerical results show that the flow patterns developing within the cavity, when the Soret number is negative, depend strongly on the thermal and solutal Rayleigh numbers: steady convection can occur with one roll (region (II) in Fig. 3). Finally, unsteady convection has been obtained for higher Rayleigh numbers, which means that the Soret number considered is lower than its critical value.

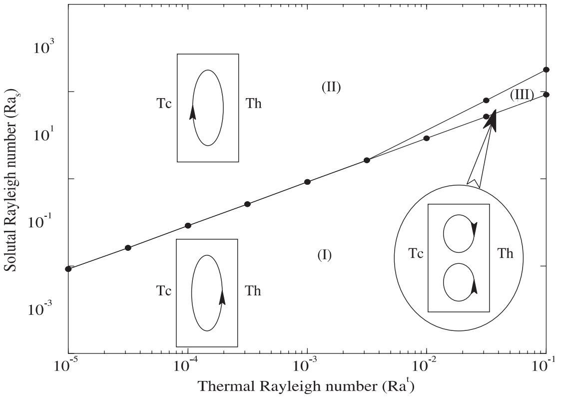

Fig. 3. Critical solutal Rayleigh numbers for which different flow patterns develop. Steamlines are shown for each flow region: (I) thermal buoyancy force is dominant, (II) solutal buoyancy force is domininant, (III) multiple convection rolls region.

For the case we are interested in, flow rapidly organises and reaches steady state. Only one convective-roll flow pattern can exist: we are modeling phenomena occurring at low thermal and solutal Rayleigh numbers, which prevents us from observing several convection rolls within the cell, as shown in Fig. 3.

4.1.2. Heat transfer

For the Rayleigh numbers we are considering, thermal and solutal buoyancy forces have no noticeable effect on heat transfer. Hence, as for convection, heat transfer rapidly reaches steady state. According to Bergman and Srinivasan [20], it quickly becomes conduction dominated (for the range of Rayleigh numbers we have considered, the thermal Peclet number is very low compared to 1). The temperature gradient across the cell is horizontal and dimensionless temperature linearly varies from 0.5 on the hot side to −0.5 on the cold side.

4.2. Mass transfer

As explained in Section 1, a discrepancy has been observed between numerical and experimental results when modeling thermogravitational experiments [30]. Therefore, we propose a short study of the combined influence of buoyancy forces and Soret effect on solute migration and distribution at steady state. However, because Section 4.1.1 shows that only one convection roll develops in the thermogravitational cells under investigation, we restrict our analysis to phenomena occurring in region (I) and (II) of Fig. 3. In addition, on the basis of theoretical developments, we exhibit the relevant parameters to the maximum steady-state separation and compare this to numerical results, which appears to be necessary in order to explain the discrepancy with experimental results.

4.2.1. Species differentiation

Negligible solutal buoyancy force; positive Soret number. Fig. 4(a)–(f) shows the solute concentration field for different times during the separation process. Originally homogeneous the differentiation progressively develops in the mixture. Horizontal concentration gradients appear first. Initially located close to the vertical walls (Fig. 4(a)), concentration gradients advance towards the cell centre (Fig. 4(b)). The gradient direction is due to the predominant solute thermal diffusive flux over the convective flux (early time convection velocity is very low). The solute being the mixture heavy component, it migrates towards the cold wall.

Convection velocity then progressively increases until steady state is reached. Therefore, solute convective flux increases and species differentiation increases as well (Fig. 4(b)–(e)), until solute diffusive, thermal diffusive and convective fluxes balance each other, which corresponds to steady state (Fig. 4(f)). This balance between the different forces is responsible for neither horizontal nor vertical direction of the steady-state concentration gradients.

Negligible solutal buoyancy force; negative Soret number. In this case, primary solute migration changes: under the influence of the Soret effect, the solute moves initially towards the hot side. Later in time during the separation process, and in agreement with Weaver and Viskanta [13], convection and thermal diffusion combine their actions to induce accumulation on the cell hot side.

Combined solutal and thermal buoyancy forces. As previously shown, a positive Soret number induce primary (e.g. early times) solute migration towards the cold cell wall (Fig. 4(a) and (b)). Term $c_s - 1$ in Eq. (9) is then positive on the cold side and negative on the hot side. As schematically shown in Fig. 5(a), solutal and thermal

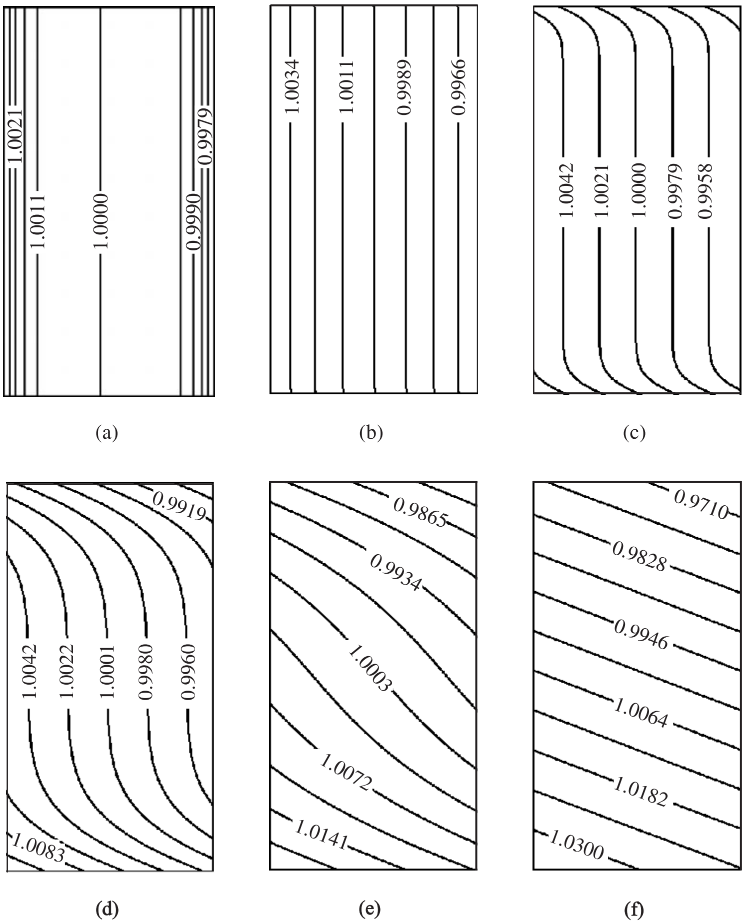

Fig. 4. Evolution of solute concentration from early time (a) to steady state (f).

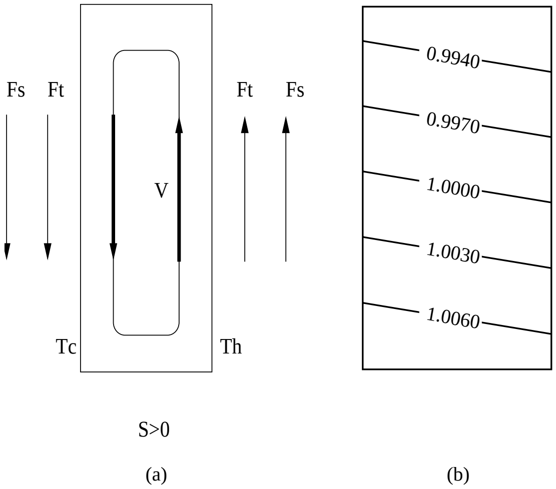

Fig. 5. (a) Schematical view of the effect of the buoyancy forces on mixture velocity for positive Soret number (F^t: thermal buoyancy force; F^s: solutal buoyancy force). (b) Solute concentration isolines obtained for: $Ra^t = 10^{-3}$, $Ra^t = 1$, $S = 1.2 \times 10^{-3}$, $HA = 100$.

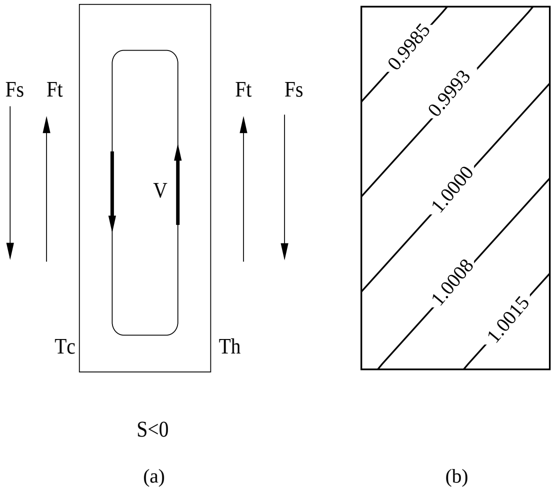

Fig. 6. (a) Schematical view of the effect of the buoyancy forces on mixture velocity for negative Soret number (F^t: thermal buoyancy force; F^s: solutal buoyancy force). (b) Solute concentration isolines obtained for: $Ra^t = 10^{-3}$, $Ra^t = 1$, $S = -1.2 \times 10^{-3}$, $HA = 100$.

buoyancy forces then combine their actions, and species differentiation is predominant (Fig. 5(b)).

Counteracting solutal and thermal buoyancy forces. Because negative Soret number induces primary solute migration towards the hot cell wall, term $c_s - 1$ in Eq. (9) is negative on the cold side and positive on the hot side at early time. Solutal and thermal buoyancy forces then have an opposing action (schematic view in Fig. 6(a)) and reduce species differentiation (Fig. 6(b)).

Note that, as shown in Fig. 6(b), solute then does not necessarily accumulate on the hot cell side, even though it is the mixture heavy component. This behaviour is opposite to the observed situation when the Soret number is negative and the solutal buoyancy force is negligible. The cell side where solute accumulation takes place depends on the direction of the convective flow when solute convective flux is higher than the combined action of diffusive and thermal diffusive fluxes.

This analysis confirms that the solutal buoyancy force, when non-negligible, can have an important effect on steady-state solute differentiation, even when only one convection roll develops in the cavity. However, thanks to the flow analysis, the thermal buoyancy force influence is the only one relevant to the phenomenon occurring in the thermogravitational cell under investigation.

4.2.2. *Solute behaviour sensitivity to dimensionless parameters*

Simplified theory. Neglecting the solutal buoyancy force and assuming constant diffusion and thermal diffusion coefficients (regarding temperature and solute concentration), low solute concentration, constant thermal gradient within the cell, two-dimensional flow within the plane defined by the thermal gradient and the cell axis, and neglecting end-wall effects, total mass transport along axis x (see Fig. 1), m_x, can be expressed in the classical form of Furry et al. [10]:

$$m_x = -\mathscr{H} c_s(1 - c_s) - \mathscr{K}\frac{\partial c_s}{\partial x}. \tag{14}$$

Steady-state solute concentration is then readily expressed, and the corresponding separation ratio, q, is

$$q = \frac{c_{sB}/(1 - c_{sB})}{c_{sT}/(1 - c_{sT})} = \exp\left(\frac{\mathscr{H}\mathrm{L}}{\mathscr{K}}\right), \tag{15}$$

where subscripts T and B, respectively, stand for cell top and cell bottom. For low solute concentration, q reduces to the ratio c_{sB} over c_{sT}. $\mathscr{H}$ and $\mathscr{K}$ are transport parameters for which Lorenz and Emery give an expression in porous medium [38,39]. These parameters are functions of the permeability, k:

$$\mathscr{H} = \mathscr{A}k \quad \text{and} \quad \mathscr{K} = \mathscr{B}k^2 + \mathscr{C},$$

where $\mathscr{A}$, $\mathscr{B}$, $\mathscr{C}$ are functions of cell and binary mixture characteristics. Using the previous expressions for $\mathscr{H}$ and $\mathscr{K}$, Eq. (15) becomes:

$$\ln(q) = \frac{\mathscr{A}\mathrm{L}k}{\mathscr{B}k^2 + \mathscr{C}}. \tag{16}$$

Putting Lorenz and Emery approximated values for $\mathscr{A}$, $\mathscr{B}$, $\mathscr{C}$ in Eq. (16) and differentiating it with respect to k, Estebe and Schott [40] show that an extremum (maximum) value for the separation ratio, $q = q_{\mathrm{m}}$, exists for the permeability value, $k = k_{\mathrm{m}}$:

$$k_{\mathrm{m}} = \frac{\mu D \Phi \sqrt{120}}{g \beta \Delta T H \rho}. \tag{17}$$

The maximum separation ratio, q_{m}, can then be obtained for this optimum permeability. With some approximations on $\mathscr{H}$ and $\mathscr{K}$ expressions, one can write:

$$\ln(q_{\mathrm{m}}) = \frac{S^{\mathrm{t}} \Delta T \mathrm{L} \sqrt{120}}{24H}. \tag{18}$$

In terms of dimensionless parameters, Eqs. (17) and (18) respectively become:

$$Ra^{\mathrm{t}}_{\mathrm{m}} = \frac{\Phi \sqrt{120}}{Le}, \tag{19}$$

$$\ln(q_{\mathrm{m}}) = \frac{S \sqrt{120}}{24HA}. \tag{20}$$

Numerical predictions. Varying the appropriate dimensionless numbers, numerical simulation results qualitatively agree with theoretical predictions for solute behaviour (Eqs. (19) and (20)).

Dimensionless Soret and Lewis numbers being fixed, the amplitude of separation mainly depends on the thermal Rayleigh number. The closer Ra^{t} to $Ra^{\mathrm{t}}_{\mathrm{m}}$, the higher the species differentiation. Fig. 7 shows numerical results regarding steady-state separation ratio for different Ra^{t}, with $S = 1.2 \times 10^{-3}$ and $Le = 680$, the solutal buoyancy force being negligible ($Ra^{\mathrm{s}} = 0$).

As shown in Fig. 8, a decreasing Lewis number induces a decreasing separation ratio: the higher the species diffusion (e.g. D_{s_0}), the lower the species differentiation. Species diffusion then tends to homogenise the mixture. On the contrary, Fig. 8 also shows that Soret effect tends to increase the separation, and this agrees with Eq. (20).

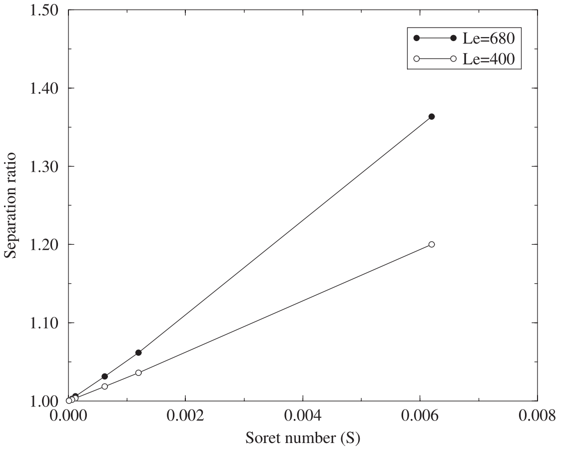

Fig. 8. Steady-state separation ratio for different Soret and Lewis numbers ($Ra^{\mathrm{s}} = 0$, $Ra^{\mathrm{t}} = 10^{-3}$, $S = 1.2 \times 10^{-2}$, $HA = 100$).

As shown in Fig. 9, the optimum Rayleigh number increases when Lewis number decreases. This qualitatively agrees with Eq. (19), but not quantitatively (compare numerical and analytical curves shown in Fig. 9). Note that optimum thermal Rayleigh number value does not depend on thermal diffusion effect, but only on diffusion (this has been verified).

For a given mixture, the maximum separation ratio obtainable depends on the cell aspect ratio (Eq. (20)). This is shown in Fig. 10 in which the steady-state separation ratio is given for different cell aspect ratios: the larger the cell aspect ratio, the higher the differentiation.

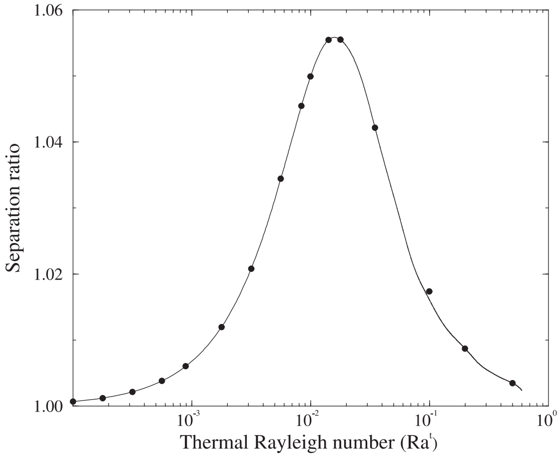

Fig. 7. Numerical steady-state separation ratio for different thermal Rayleigh numbers ($Ra^{\mathrm{s}} = 0$, $S = 1.2 \times 10^{-3}$, $Le = 680$, $HA = 100$).

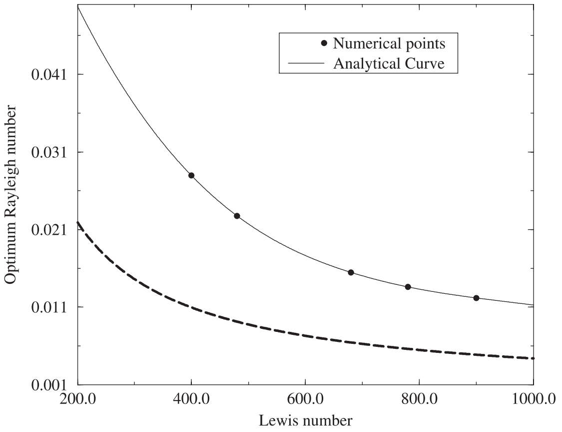

Fig. 9. Optimum Rayleigh number for different Lewis numbers ($Ra^{\mathrm{s}} = 0$, $S = 1.2 \times 10^{-2}$, $HA = 100$).

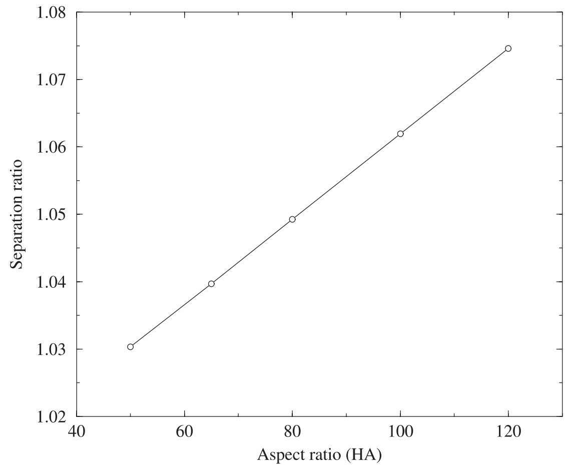

Fig. 10. Steady-state separation ratio for different cell aspect ratios ($Ra^s = 0$, $Ra^t = 10^{-3}$, $S = 1.2 \times 10^{-2}$, $Le = 680$).

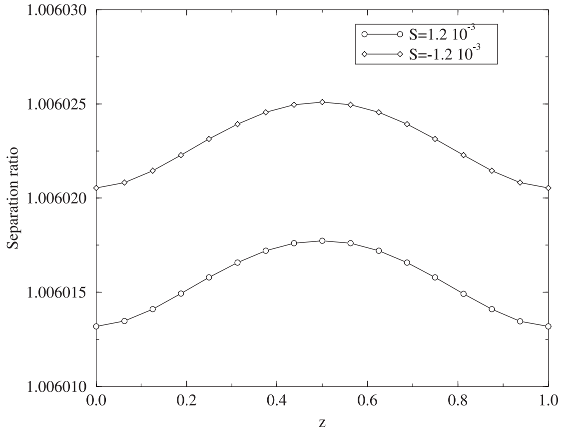

Fig. 11. Steady-state separation ratio for positive Soret number and inverse of separation ratio for negative Soret number: evolution along axis z. ($Ra^s = 10^{-5}$, $Ra^t = 10^{-3}$, $Le = 680$, $HA = 100$).

Changing Soret number sign inverts the separation process (Eq. (20)). This has been verified when the solutal buoyancy force is negligible, but if this force is of some importance, it is no longer true. Even if the solute is the mixture heavy component, it has been shown in Fig. 6(b) that for a negative Soret number, its accumulation can take place on the cold cell side.

According to Eq. (20), when the Soret number sign changes, the "amplitude" of differentiation in the cell remains the same: q_m for $S < 0$ takes the value $1/q_m$ for $S > 0$, which implies that solute concentration field is inverted. This has only been verified for negligible solutal buoyancy force (Fig. 11, and it might not be true all the time.

4.3. Comparison with experiments

4.3.1. Experimental procedure and results

Rather than developing in detail the experimental procedure, our purpose is to present an overview of the procedure: our principal goal is to model these experiments.

Soret-number measurement experiments are done using thermogravitational cells [6], originally developed by Clusius and Dickel [27,28]. The apparatus is made of a cylindrical cell. Inside there is an inner tube through which hot water flows. The cold cell wall is then the external boundary. Both temperatures are kept constant during the experiment. The porous medium is made of an artificial corindon grains (Al_2O_3). Porosity and permeability are then accurately known for each experiment, depending on the grain size and packing. Cell height and length are, respectively: $L = 0.4$ m and $H = 0.004$ m.

The fluid studied is water, for which composition is given in Table 1: it can either be considered as the binary mixture $H_2^{16}O$–$HD^{16}O$ or $H_2^{16}O$–$H_2^{18}O$, the solutes being, respectively, $HD^{16}O$ or $H_2^{18}O$. Small fluid samples are taken at the cell top and bottom using hypodermic needles, so that (i) flow is not disturbed, (ii) samples are not contaminated, and (iii) the sample temperature is identical and equal to T_0: the composition difference between cell top and bottom is then only due to thermogravitation. Their composition is determined by measuring isotopic abundance of deuterium or ^{18}O using mass spectrometry.

Soret number computation is based on Eqs. (17) and (18). Because the optimum permeability is not known a priori, Estebe and Schott [40] suggest performing l experiments with l solid matrices (permeability k_l). The steady-state separation ratio for each experiment, q_l, is then experimentally known, and $q_l = f(\log(k_l))$ can be plotted. With this curve being a gaussian type curve (see Eq. (16) and the numerical results in Fig. 7), we can

Table 1
Pure water composition

Component	$H_2^{16}O$	$D_2^{16}O$	$HD^{16}O$	$H_2^{18}O$	$HD^{18}O$	$D_2^{18}O$
Composition (%)	0.9973	0.243×10^{-7}	0.1556×10^{-3}	0.001979	0.309×10^{-6}	0.482×10^{-10}

graphically determine the maximum separation ratio and the corresponding permeability. The solute Soret number is then calculated using Eq. (18). The more experiments, the more accurate the Soret-number evaluation.

Several sets of experiments, corresponding to different temperature gradients, have been conducted. In the following, we only consider the set corresponding to an average temperature of 47.5°C. The solid–matrix and mixture characteristics are given in Table 2. For each set, the porous medium permeability is the only parameter that varies from one experiment to another (this is achieved by changing the corindon grain size to make the porous medium). Accurate values for $HD^{16}O$ and $H_2^{18}O$ Soret numbers have been determined. Experimental results regarding optimum permeability, corresponding steady-state separation ratio and Soret coefficients, are shown in Table 3, with the experimental uncertainty regarding permeability and the corresponding Soret number values.

4.3.2. Modeling the experiments

In order to model experiments by numerical means, the water solutal expansion coefficient, $\alpha = (1/\rho_{f_0})(\partial\rho_f/\partial c_s^*)_{T^*}$, has to be known. Regarding the considered solutes, the literature does not give any special value for this number. We are therefore assuming $\alpha = 0$: the water density variations are negligible regarding solute concentration variations. The solutal Rayleigh number is then $Ra^s = 0$ for both solutes.

To calculate the Lewis number, which is an important parameter in the separation process (see Fig. 8), mean-temperature equivalent thermal conductivity, λ_0^{eq}, has to be determined. In a two-phase system, say γ and δ, assuming that one phase is continuous (say γ), Maxwell's formula permits the computation the equivalent thermal conductivity [41]:

$$\lambda^{eq} = \lambda_\gamma \frac{3\kappa - 2\phi_\gamma(\kappa - 1)}{3 - \phi_\gamma(\kappa - 1)}, \tag{21}$$

where $\kappa = \lambda_\delta/\lambda_\gamma$ and ϕ_γ is the relative volume of phase γ.

Extreme values for λ^{eq} then correspond to γ continuous and δ continuous, respectively.

Water thermal conductivity at $T_0 = 47.5°C$ being $\lambda_{water} = 0.64\ W\ m^{-1}\ K^{-1}$ (Handbook of Chemistry, 1976), λ_0^{eq} lies within the range:

$$2.89\ W\ m^{-1}\ K^{-1} \leqslant \lambda_0^{eq} \leqslant 9.27\ W\ m^{-1}\ K^{-1}.$$

For $HD^{16}O$, the Lewis numbers corresponding to this range of thermal conductivity are:

$$334 \leqslant Le \leqslant 1073$$

(water heat capacity is $4.18005 \times 10^3\ J\ g^{-1}\ K^{-1}$ at T_0). Considering $HD^{16}O$ Soret number, the maximum separation ratio numerically obtained for this range of Lewis numbers is close to the experimental one:

$$1.0558 \leqslant q_m^{num} \leqslant 1.0559.$$

Reading from Fig. 9 the optimum thermal Rayleigh numbers corresponding to this range of Lewis numbers, it is:

$$0.0107 \leqslant Ra_m^t \leqslant 0.0336.$$

It is then possible to back-calculate the numerical optimum permeability, k_m^{num}:

$$4.13 \times 10^{-11}\ m^2 \leqslant k_m^{num} \leqslant 4.22 \times 10^{-11}\ m^2.$$

Experimental is then higher than the numerical optimum permeability (see Table 3).

Similar results are obtained when considering pure water as the mixture $H_2^{16}O$–$H_2^{18}O$.

4.3.3. Influence of dispersion

Although the amplitude of differentiation is calculated well, the numerical model does not correctly predict optimum permeability values. Costesèque [6] noticed that such a theory presented drawback, and Jamet et al. [30] also pointed out this problem when using his numerical model. They tried [30] to explain the

Table 2
Experiment and mixture characteristics

Matrix		Mixture					
Φ (%)	$\lambda_{Al_2O_3}$ (W m^{-1} K^{-1})	ΔT (°C)	β (°C^{-1})	μ (Pa s)	ρ (kg m^{-3})	$D_{HD^{16}O}$ (m^2 s^{-1})	$D_{H_2^{18}O}$ (m^2 s^{-1})
40	17.75	19	4.4×10^{-4}	5.7×10^{-4}	989.1	2.09×10^{-9}	2.67×10^{-9}

Table 3
Experimental results regarding Soret number measurements

	k_m (m^2)	Δk	q_m	S	ΔS
$HD^{16}O$	8.76×10^{-11}	0.05×10^{-11}	1.056	1.2×10^{-3}	9.5×10^{-5}
$H_2^{18}O$	8.96×10^{-11}	0.05×10^{-11}	1.041	8.9×10^{-4}	9.5×10^{-5}

observed discrepancy by considering an anisotropic porous medium. However, it did not have the expected corrective effect. Later, Fargue et al. [42] proposed that a dispersion phenomenon acts on the thermal coefficient D^t, compared with the well-known dispersion coefficient associated with the diffusion coefficient in porous medium.

We therefore propose a similar analysis for the observed discrepancy. By means of homogenisation from the pore scale to the macroscopic scale, Arquis and Caltagirone [43] studied the influence of dispersion on species transport. For the porous media they considered, they showed that dispersion can strongly affect mass transport as a peak of the convection velocity magnitude. Species intrinsic diffusion coefficients are therefore no longer relevant to the problem and have to be updated to take account of dispersion.

The solutal Peclet number is the relevant parameter for dispersion effects on mass diffusion: $Pe^s = ReSc$, where is the Reynolds, Re, and the Schmidt, Sc, numbers. For a given Reynolds number ($Re = 7.25 \times 10^{-3}$), dependence of D_s and D_s^t on dispersion is shown in Fig. 12 for a porous medium porosity equal to 0.75 and a thermal Peclet number, $Pe^t = 1.74 \times 10^{-3}$. The higher the Schmidt number, $Sc = \nu/D_{s_0}$, the higher the actual diffusion and thermal diffusion coefficients, respectively, D_d and D_d^t (these numbers then include dispersion effects). As shown, effect of dispersion on mass diffusion coefficients can be strong.

For the mixtures we consider, the Schmidt numbers are:

$$Sc_{HD^{16}O} = 275.73 \quad \text{and} \quad Sc_{H_2^{18}O} = 215.84.$$

According to Fig. 12, values for the diffusion coefficients taking dispersion into account are $D_d > D_s$ and $D_d^t > D_s^t$. Considering this change in the diffusion coefficient due to dispersion, there is a new value for Le, lower than the one obtained with D_s0. As shown in Fig. 9, optimum Rayleigh number increases when Lewis number decreases. Therefore, taking dispersion into account, this should allow us to obtain, by numerical calculations, the experimental value for the optimum permeability.

Let us do the following calculations. Knowing the experimental optimum permeability, the corresponding experimental optimum Rayleigh number can be calculated. Assuming that this value is the one that should be obtained by numerical calculations (if the dispersion was correctly handled), it is possible to use the results reported in Fig. 9 to obtain an evaluation for the Lewis number. This procedure leads to:

$$Le_{HD^{16}O} = 328 \quad \text{and} \quad Le_{H_2^{18}O} = 320.$$

Then, back-calculating the actual diffusion coefficients (for an average value of the equivalent thermal conductivity):

$$D^*_{HD^{16}O} = 4.48 \times 10^{-9}\ \text{m}^2\ \text{s}^{-1} \quad \text{and}$$

$$D^*_{H_2^{18}O} = 4.6 \times 10^{-9}\ \text{m}^2\ \text{s}^{-1}.$$

Using these diffusion–dispersion coefficients to model the experiments (e.g. the corresponding Lewis numbers), good results are obtained, either for HDO or $H_2^{18}O$: Fig. 13 shows numerical and experimental results for both solutes. As expected, once mass diffusion is well computed, the numerical model perfectly fits the experimental results.

However, one can put forward that the dispersion effect on solute diffusion and thermaldiffusion is, firstly, low for the Schmidt numbers corresponding to the experiment and, secondly, similar on both diffusion

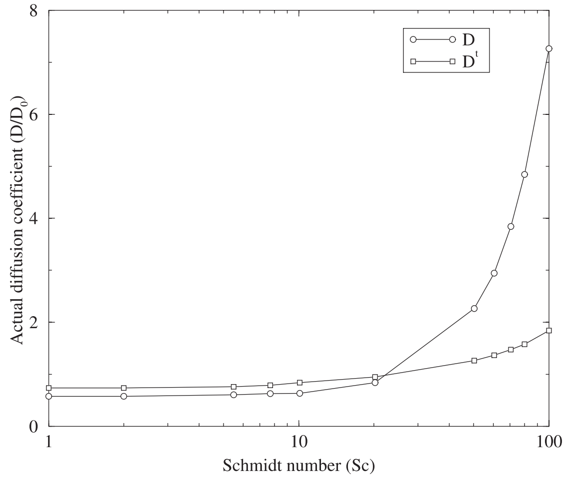

Fig. 12. Diffusion, D, and thermal diffusion, D^t, coefficients as a function of Schmidt number (from [43]).

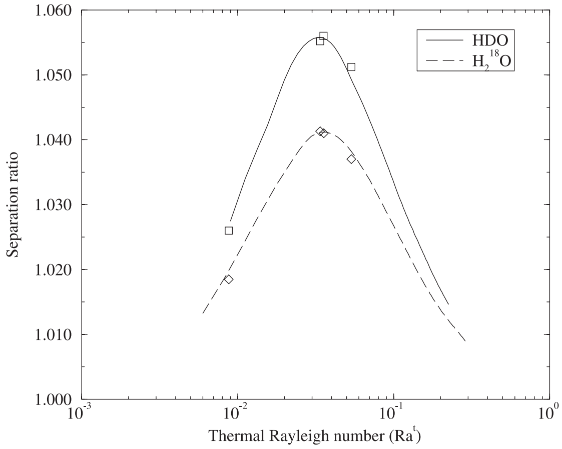

Fig. 13. Numerical results obtained when considering dispersion phenomena. Symbols are for experimental results.

phenomena, which do not correspond to the results shown in Fig. 12. Actually, the results by Arquis and Caltagirone [43] correspond to a higher porosity (75% against 40%), a higher Reynolds number (7.35×10^{-3} against 4.30×10^{-3}) and a higher thermal Peclet number (7.25×10^{-3} against 1.74×10^{-3}) than the experimental ones. Therefore, for the experiment we model, dispersion is effective but has to be lower than the one shown in Fig. 12: the diffusion coefficients are increased by 115% for HDO and 75% for $H_2^{18}O$ to obtain coefficients including dispersion effect.

5. Conclusions

Aiming at modeling thermogravitational experiments, we have addressed the problem of thermal diffusion in binary mixtures lying within a porous medium (in a particular configuration). Hence, we have first shown that multiple convection-roll flow patterns can develop when solutal and thermal buoyancy forces oppose each other, depending on the Soret number value.

Investigating solute behaviour, we can explain how differentiation occurs depending on the previous forces, and can show that generally accepted solute behaviour is not necessarily verified for counteracting forces (e.g. negative Soret number when the solutal expansion coefficient is positive). Achieving a sensitivity study, the importance of cell aspect ratio, species interdiffusion and permeability for separation process is shown, in qualitative agreement with the theory.

Finally, with the intention of reproducing the thermogravitational experiments, we observe a discrepancy between numerical and experimental results when evaluating the optimum permeability for solute separation. We then show that dispersion can be responsible for this phenomenon, and that it can strongly affect diffusive and thermal-diffusive coefficients.

References

[1] C. Soret, Influence de la température sur la distribution des sels dans leurs solutions, Compte-Rendu de l'Académie des Sciences, Paris 91 (1880) 289–291.

[2] A. Rice, The mechanism of Mt. St. Helens eruption and speculations regarding Soret effect in planetary dynamics, Geophysical Surveys 7 (1985) 303–384.

[3] C.R. Carrigan, R.T. Cygan, Contribution of Magma chamber dynamics to Soret fractionation, in: The Geological Society of America; 98th Annual Meeting, vol. 17, The Geological Society of America, 1985, p. 539.

[4] V.A. Pugin, N. Bagdasarov, The Soret effect as a possible cause of Magma differentiation, Geochemistry International 25(4) (1988) 57–65 (Trans. From Geokhimiya, No. 9, 1987, 1285–1294).

[5] P. Costesèque, Sur la migration des eléments par thermodiffusion. Etat et perspectives d'un modèle géochimique, Bulletin de Minéralogie 108 (1985) 305–324.

[6] P. Costesèque, Sur la Migration sélective des isotopes et des eléments par thermodiffusion dans les solutions. Application de l'effet thermogravitationnel en milieu poreux; observations expérimentales et conséquences géochimiques, Ph.D. Thesis, Université Paul Sabatier, Toulouse, France, 1982.

[7] P. Costesèque, M. Hridabba, J. Sahores, Possibilité de différenciation des hydrocarbures par diffusion thermogravitationnelle dans un pétrole brut imprégnant un milieu poreux, Compte-Rendu de l'Académie des Sciences, Paris 304 (II-17) (1987) 1069–1074.

[8] P. Costesèque, M. El Maataoui, J. Sahores, Sur la différenciation des hydrocarbures constituant la fraction légère d'un brut par thermodiffusion gravitationnelle en milieu poreux, Compte-Rendu de l'Académie des Sciences, Paris 305 (II) (1987) 1531–1536.

[9] C.E. Lesher, D. Walker, Thermal Diffusion in Petrology, vol. 8, Advances in Physical Geochemistry, 1991, pp. 396–451 (Chapter 12).

[10] W.H. Furry, R.C. Jones, L. Onsager, On the theory of isotope separation by thermal diffusion, Physical Review 55 (1939) 1083–1095.

[11] S.R. De Groot, Theorie phénoménologique de l'effet Soret, Physica 9 (7) (1942) 699–708.

[12] S.R. De Groot, P. Mazur, Non Equilibrium Thermodynamics, North-Holland Publishing Company, Holland, 1962.

[13] J.A. Weaver, R. Viskanta, Natural convection due to horizontal temperature and concentration gradients – 2. Species interdiffusion, Soret and Dufour effects, International Journal of Heat and Mass Transfer 34 (12) (1991) 3133–3133.

[14] G. Zimmerman, U. Müller, Benard convection in a two-component system with Soret effect, International Journal of Heat and Mass Transfer 35 (9) (1992) 2245–2256.

[15] W. Barten, M. Lücke, M. Kamps, R. Schmitz, Convection in binary fluid mixtures. {II} Localized travelling waves, Physical Review E 51 (6) (1995) 5662–5680.

[16] C. Karcher, U. Müller, Onset of oscillatory convection in binary mixtures with Soret effects and solidification, International Journal of Heat and Mass Transfer 37 (16) (1994) 2517–2523.

[17] J.K. Platten, J.C. Legros, Convection in Liquids, Springer, Berlin, 1984.

[18] D.P. Chock, C.-H. Li, Direct integration method applied to Soret driven instability, Physics Fluids 18 (1975) 1401–1406.

[19] G. Zimmerman, Benard-konvektion in binären flüssigkeitsmischungen mit thermodiffusion, Ph.D. Thesis, Univrsität Karlsruhe und KfK 4683, Germany, 1990.

[20] T.L. Bergman, R. Srinivasan, Numerical simulation of Soret-induced double diffusion in an initially uniform concentration binary liquid, International Journal of Heat and Mass Transfer 32 (4) (1989) 679–687.

[21] D.T. Hurle, E. Jakeman, Soret-driven thermosolutal convection, Journal of Fluid Mechanics 447 (1989) 667–687.

[22] B. Hafskjold, T. Ikeshoji, S.K. Ratkje, On the molecular mechanism of thermal diffusion in liquids, Molecular Physics 80 (6) (1993) 1389–1412.

[23] K.J. Zhang, M.E. Briggs, J.V. Sengers, Optical measurement of the Soret coefficient and the diffusion coefficient of liquid mixtures, Journal of Chemical Physics 104 (17) (1996) 6881–6892.

[24] P. Kolodner, H. Williams, C. Moe, Optical measurement of the Soret coefficient of ethanol/water solutions, Journal of Chemical Physics 88 (10) (1988) 6512–6524.

[25] J.P. Praizey, S. Van Vaerenbergh, J.P. Garandet, Thermomigration on board EURECA, Advances in Space Research 16 (7) (1995) (7)205–(7)214.

[26] S. Van Vaerenbergh, J.-Cl. Legros, J-Cl. Dupin, First results of Soret coefficient measurement experiment, Advances in Space Research 16 (8) (1995) (8)69–(8)81.

[27] K. Clusius, G. Dickel, New process for separation of gas mixtures and isotopes, Naturwissenschaften 26 (1938) 546.

[28] K. Clusius, G. Dickel, The separating tube process for liquids, Naturwissenschaften 27 (1939) 148–149.

[29] E. Rivière, P. Costesèque, Sur la diffusion thermogravitationnelle een milieu poreux dans une huile naturelle: influence de la fraction légère d'un brut sur l'Ampleur des migrations et estimation des coefficients de Soret des principaux composants de la Fraction Légère, Compte-Rendu de l'Académie des Sciences, Paris, 315(II) 179–185.

[30] P. Jamet, D. Fargue, P. Costesèque, G. De Marsily, A. Cernes, The thermogravitational effect in porous media: a modelling approach, Transport in Porous Media 9 (1992) 223–240.

[31] M. Fortin, R. Glowinsky, Méthode de Lagrangien augmenté. Application à la résolution des problèmes aux limites, Dunod, Méthode Numérique de l'informatique, 1982.

[32] H. Uzawa, Studies in Linear and Nonlinear Programming, chapter Iterative methods for concave programming, Stanford University Press, Stanford, CA, 1958, pp. 154–165.

[33] X. Nicola, P. Traore, A. Mojtabi, J.P. Caltagirone, Augmented lagrangian method and open boundary conditions in 2D simulation of Poiseuille–Bénard channel flow, International Journal of Numerical Methods and Fluids 25 (3) (1997) 265–283.

[34] J.B. Ritz, J-P. Caltagirone, A numerical continuous model for the hydrodynamics of fluid particle systems, International Journal of Numerical Methods and Fluids 30 (8) (1999) 1067–1090.

[35] S. Vincent, J.-P. Caltagirone, Efficient solving method for unsteady incompressible interfacial flow problems, International Journal of Numerical Methods and Fluids 30 (6) (1999) 795–811.

[36] S.V. Patankar, Numerical Heat Transfer and Fluid Flow, Hemisphere, New York, 1990.

[37] H.A. Van der Vorst, BI-CGSTAB: A fast and smoothy converging variant of BI-CG for the solution of nonsymetric linear systems, SIAM Journal of Scientific and Statistical Computing, vol. 13, pp. 631–644.

[38] M. Lorenz, A.H. Emery, The packed thermal diffusion column, Chemical Engineering Science 11 (1959) 16–23.

[39] A.H. Emery, M. Lorenz, Thermal dissusion in a packed column, Chemical Engineering Journal 9 (5) (1963) 661–663.

[40] J. Estebe, J. Schott, Concentration des solutions salines et cristallisation dans les milieux poreux par effet thermogravitationnel, Compte-Rendu de l'Académie des Sciences, Paris, 1970.

[41] M. Quintard, S. Whitaker, Transport in ordered and disordered porous media: volume-averaged equations, closure problems, and comparison with experiment, Chemical Engineering Science 48 (14) (1993) 2537–2564.

[42] P. Jamet, D. Fargue, P. Costesèque, Determination of the effective transport coefficients for the separation of binary mixtures of organic compounds into packed thermal diffusion columns, Chemical Engineering Science 51 (19) (1996).

[43] E. Arquis, J.-P. Caltagirone, Détermination numérique des coefficients de thermodiffusion effectifs en milieux poreux par une approche à une échelle locale, Entropie 198–199 (1996) 39–44.